

Description of boiling mechanisms in quiescent medium using biphilic surfaces

Ricardo Miguel Mendes Cautela

ricardo.m.cautela@tecnico.ulisboa.pt

Instituto Superior Técnico, Universidade de Lisboa, Portugal

June 2019

Keywords: Biphilic surfaces, wettability, pool boiling, bubble dynamics, heat transfer

Abstract

The present work addresses the impact of wettability in pool boiling heat transfer and explores the potential increase in heat transfer coefficients, claimed by a few authors, when using the so-called biphilic surfaces, i.e. hydrophilic/superhydrophilic surfaces with hydrophobic/superhydrophobic regions. In the light of the consulted literature, a methodical approach towards the development of biphilic patterns is not yet available. Hence, this study engages in a systematic analysis of the influence of the geometry of biphilic arrangements on bubble dynamics and the heat transfer processes that occur in pool boiling conditions. The superhydrophobic regions are prepared by altering the surfaces' chemical properties and topography.

Parameters like the size of the superhydrophobic regions and the spacing between them are systematically varied and their consequent effect is analyzed in both bubble dynamics and heat transfer processes. The required data is obtained based on extensive post-processing of images taken using synchronized high-speed video and time and spatially resolved thermography. Varying the size of the superhydrophobic regions is observed to alter significantly bubble dynamics and the evaporated mass flux. Results show that the configuration with the smallest superhydrophobic regions is more effective at removing heat through evaporation. As for the spacing between regions, the data supports that the optimum distance is the one providing moderate coalescence between bubbles. For such distance (approximately the diameter of the superhydrophobic regions) the bubbles do not interact near the surface and promote continuous induced flow between superhydrophobic regions, cooling the surface.

Introduction

Over the years, research has been made in order to study the influence of changing surface parameters in the pool boiling heat transfer. Early on it has been found that the variation in certain surface properties increased its heat transfer ability at relatively low superheat temperatures. Wettability, which basically quantifies the way the liquid spreads on a surface, has proved, for several decades, an essential factor to be considered in the study of the factors that affect nucleation since it is linked to the bubble dynamics process [1]. However, there is no explicit and systematic method to quantificate its effect on the pool boiling heat transfer mechanisms.

Recent studies have applied micro and nanometric manufacturing techniques to modify the topography of a surface with great precision and consequently its wettability [2]. From the several ways to vary the wettability of a surface, usually quantified by the static contact angle (θ_s), this work considers the effects of the simultaneous modification of the chemistry and the topography of a surface. In the literature, it is reported that the use of superhydrophobic surfaces under pool boiling conditions allows nucleation to reach a superheat temperature considerably lower than those reached in the case of hydrophilic surfaces [3]. However, the heat transfer coefficients associated with the superhydrophobic surfaces are smaller, since a

vapor film forms on the surface prematurely and performs as thermal insulator. To overcome this problem, the so-called biphilic surfaces started to be tested. These surfaces combine areas with different types of wettability, namely hydrophilic ($\theta_s < 90^\circ$) or superhydrophilic ($\theta_s = 0^\circ$) surfaces with hydrophobic ($\theta_s > 90^\circ$) or superhydrophobic ($\theta_s > 150^\circ$) regions. By employing the use of biphilic surfaces it is possible to achieve nucleation at lower superheat temperatures and to prevent early coalescence between bubbles and consequent uncontrolled vapor buildup on the surface. Through experimental tests, recent studies show that these surfaces provide higher heat transfer coefficients than those previously mentioned, i.e. hydrophilic and hydrophobic surfaces [4] [5]. In these studies, several biphilic patterns were evaluated in terms of the superhydrophobic regions diameter, the spacing between regions and the ratio between the hydrophilic and superhydrophobic areas. However, in spite of the good results promoted by these surfaces, the biphilic patterns studied are generally shaped in a somewhat random way, as their relation with the bubble dynamics and the heat transfer processes weren't considered. In this context, some authors argue that a more systematic and focused analysis on the geometric parameters is needed, as bubble dynamics plays a vital role in an efficient process to devise such biphilic surfaces (e.g. [6], [7]). The effect of bubble dynamics on these surfaces and their complex association with

the heat transfer mechanisms needs to be more broadly described and understood in greater detail. Within this scope, the present work concerns the detailed characterization of the bubble dynamics on biphilic surfaces towards the development of an optimum biphilic pattern, in order to enhance pool boiling heat transfer at reduced surface superheat.

Following the considerations of previous studies (e.g. [8], [9]), this work employs basic patterns with one, two and three superhydrophobic regions and evaluates the effects of these regions' size and the distance between them. The connection between bubble dynamics and heat transfer processes is explored by combining the visualization and processing of images obtained with a high-speed camera and a high-speed infrared camera. These images are processed by adapting the procedures and algorithms initially developed by Pontes [10].

Experimental setup and procedures

Experimental setup

Figure 1 shows, in a schematic way, the essential components responsible for the general operation of the experimental setup.

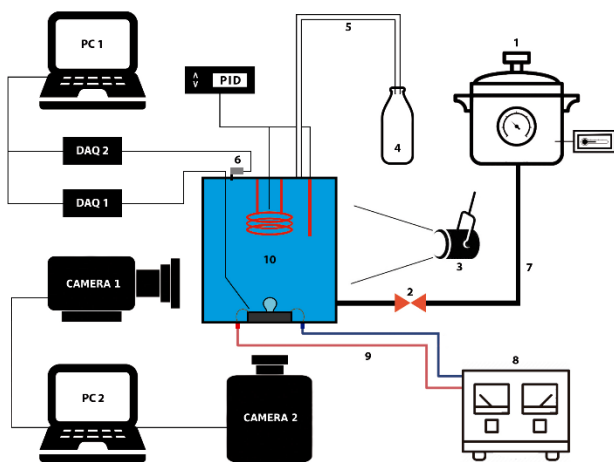


Figure 1: Schematic representation of the experimental setup: (1) Degasification station, (2) Valve, (3) LED, (4) Condensate container, (5) Vapor outlet tube, (6) Pressure transducer, (7) Inlet water tube, (8) DC Power Supply, (9) Electrical cables, (10) Main tank

The core component to consider is the main tank (10), which is filled with pre-heated and degassed distilled water by the degassing station (1). The water is maintained at the saturation temperature with the aid of two electrical resistances, a PID controlled cartridge heater and a coil heater.

Considering that the tank is an open system, a tube has been placed on its top (5) in order to redirect the generated water vapor to a container (4), where it condenses.

The distilled water flows out of the degassing station into the tank via a tube (7), which is covered by an insulating sleeve and controlled by a valve (2).

Two K type thermocouples and an OMEGA DYNE INC pressure transducer (6) are used to control the working conditions inside the main tank, which are constantly monitored during the use of the experimental setup. The information taken from these sensors passes through two data readers (DAQ 1 and 2) to a computer (PC 1).

At the base of the tank is located the biphilic test surface where the nucleation phenomena will be observed. This surface is made from stainless-steel (AISI304) and is heated by Joule effect when fed by an HP6274B DC Power Supply (8), in order to promote a controlled nucleate boiling. The observed phenomena are recorded by a Phantom v4.2 high-speed camera (Camera 1), which is located right next to one of the tank's windows. In the opposite window is installed a LED (3) that illuminates the interior of the tank.

Index 9 represents the electrical cables that are linked to the connectors of the tank's base and transmit the electric current.

The test surface has an electrical resistance of 0.052Ω and a very reduced thickness of $20 \mu\text{m}$, so that a high-speed IR camera (Camera 2), mounted underneath it, can capture thermographic images of the surface temperature variation. The surface thickness was selected after some test trials and following the recommendations of Sielaf [11].

The images captured by both cameras are viewed in real time on a second computer (PC 2).

Surface preparation

The biphilic surfaces were prepared according to the following steps:

1. A stainless-steel sheet (AISI304) was cut to a defined dimension (50x38 mm);
2. Two small blocks of steel were duly sanded, cleaned and then welded to two copper wires;
3. A thin layer of silicone was placed on the face of the thermal glass where the test surface was glued.
4. The free ends of the copper wires were fixed to an electrical connector properly isolated from the stainless-steel base of the vessel with ceramic washers.
5. There were made one, two or three holes with well-defined diameters on a PVC tape strip.
6. The selected strip was placed on the surface in a way to enable the IR camera to collect accurate images.
7. Several layers of a superhydrophobic spray (Neverwet-RustOleum) were deposited on the strip. The previously prepared PVC strip thus served as a stencil to prepare the biphilic patterns.
8. After 12 h of spraying the last layer, the PVC tape was removed revealing one or more well-defined superhydrophobic circular areas.

In the tested configurations, in order to evaluate the bubble dynamics, the diameter of the

superhydrophobic regions is varied: $\phi = \{1,5 \text{ mm}; 2,6 \text{ mm}; 5,2 \text{ mm}\}$. In the biphilic configurations where the interactions between two bubbles were analyzed, the distance between the regions was varied as follows: $\delta = \{0,5 \phi; 1 \phi; 2 \phi\}$. In the latter case, only one diameter was used, chosen after the analysis of the unique bubble dynamics. For the configuration with three superhydrophobic regions both ϕ and δ have already been defined.

Characterization of the surfaces

The biphilic surfaces used in this work were characterized in terms of wettability and topography, as described in the following paragraphs. The wettability is quantified by measuring the static (θ_s), quasi-static advancing (θ_a) and receding (θ_r) contact angles and the hysteresis ($\Delta\theta$). These angles were obtained using the optical tensiometer (THETA-Attension).

To obtain the quasi-static advancing angles a droplet was deposited on the surface, then slowly enlarged and the first measurement of the angle was recorded when the liquid-solid contact line moved. The quasi-static receding angle was measured in the same way but by withdrawing volume from the droplet and waiting for the retreat of the contact line. The hysteresis is represented by the difference between θ_a and θ_r . The values obtained show that the areas painted with the Neverwet spray have a superhydrophobic behavior ($\theta_s > 150^\circ$ e $\Delta\theta < 10^\circ$) and that the hydrophilic areas also have the expected results ($\theta_s < 90^\circ$).

In order to quantify the topography in the superhydrophobic regions the stochastic roughness was analyzed using a Dektak3-Veeco profilometer, with a maximum vertical resolution of 200 Å. A diamond probe was placed and dragged along the test surface, thus measuring the roughness profile. The obtained profiles were then processed in order to obtain the values of the mean roughness (R_a) and the mean peak-to-peak roughness (R_z) which is the average of the highest peaks measured in one scan, calculated according to standard DIN4768. At least five measurements were performed where $R_a = 5,8 \mu\text{m}$, with a standard deviation of 1,5 μm , and $R_z = 22,6 \mu\text{m}$, with a standard deviation 3,9 μm . The values of R_a and R_z for the hydrophilic areas were recorded as zero within the resolution of the equipment, whereby the roughness of these regions is negligible.

To complement the information provided by the profilometer a qualitative analysis of surface topography was also performed, using a Leica SP8 Confocal Microscope. Based on the images obtained from this device it is possible to confirm the regularity in the topography of the superhydrophobic surface.

Pool boiling tests

The experimental conditions imposed during the tests inside the main tank were continuously monitored and recorded, namely, a saturation temperature of $273,5 \pm 3 \text{ K}$, measured near the test surface, a pressure

of $1000 \pm 10 \text{ mbar}$ and an adjustable heat flux on that same surface.

Four different current intensity values were chosen to be imposed on the test surface: $I = \{3 \text{ A}; 5 \text{ A}; 7 \text{ A}; 9 \text{ A}\}$, corresponding to four different heat flux values: $q'' = \{0,03 \text{ W/cm}^2; 0,07 \text{ W/cm}^2; 0,13 \text{ W/cm}^2; 0,22 \text{ W/cm}^2\}$.

The high-speed camera collected images for two different types of experiments. Long-term tests (20 min) to measure the bubble departure frequency for the different biphilic configurations and for the four different heat fluxes values. For these tests the number of bubbles that departed from the surface in a time period of 40,5 s were counted, for every 2 min, during 20 min. The period used was defined based on the maximum recording time of the high-speed camera within the used settings. The other test consisted of recording short videos, at 2200 frames/s and lasting up to 6 s, in order to infer on the bubble dynamics history. For these tests the referred four different heat flux values were used again.

Thermographic videos of the stainless-steel sheet's bottom surface were recorded with the IR camera, lasting approximately 10 s. In these videos was clearly visible the temperature distribution map of the bubbles formed on the superhydrophobic regions. The stainless-steel sheet's bottom surface was painted black to place its emissivity near 1 and to avoid camera viewing reflection.

These videos were recorded synchronously, with the same image acquisition rate ($\approx 1600 \text{ frames/s}$), along with new videos from the high-speed camera. A low integration time (200 ms) was used in order to obtain more information in the desired temperature range, although slightly increasing image noise. The size of the pixel depends on the optical arrangement used. For the cases considered here, the best pixel size was 100 μm for the IR arrangement and 50 μm for the high-speed arrangement.

In both cases, MATLAB algorithms, developed and detailed in earlier works (e.g. [10] e [12]), were used to process the thermographic and bubble dynamics images respectively.

Uncertainties

Table 1 shows the maximum relative errors associated with the bubble dynamics parameters for biphilic configurations with three different SHF areas, with $q'' = 0,22 \text{ W/cm}^2$. The parameter d_{max} refers to the maximum bubble diameter and θ_{min} represents the minimum dynamic contact angle.

Table 1: Uncertainty of the bubble dynamics parameters for biphilic configurations with three SHF areas

SHF region diameter	$e[d_{max}]$ (%)	$e[\theta_{min}]$ (%)
$\phi = 1,5 \text{ mm}$	7,8	26,5
$\phi = 2,6 \text{ mm}$	4,8	12,9
$\phi = 5,2 \text{ mm}$	7,8	10,6

Table 2 shows the relative errors associated to the mean bubble departure frequency (f) measured for each biphilic configuration with one superhydrophobic region and for four different current intensity values. The data presented serve as reference for other tests performed with multiple superhydrophobic regions.

Table 2: Uncertainty of the mean of the bubble departure frequencies, measured for each SHF region diameter and for each current intensity measurement

SHF region diameter	$e[f_{3A}]$ (%)	$e[f_{5A}]$ (%)	$e[f_{7A}]$ (%)	$e[f_{9A}]$ (%)
$\phi = 1,5 \text{ mm}$	25,7	15,1	30,3	22,9
$\phi = 2,6 \text{ mm}$	13,2	17,9	20,1	24,3
$\phi = 5,2 \text{ mm}$	-	25,5	16,4	10,1

Results and Discussion

Analysis of the bubble dynamics and thermography in a superhydrophobic region with fixed diameter

Firstly, experiments were performed on a biphilic surface with a single circular superhydrophobic region, measuring 1,5 mm in diameter. The heat flux was varied, and its effect was observed in terms of the dynamic behavior of the developing bubbles and the heat transfer mechanisms. As described in the previous chapter, applying a rising heat flux from $q'' = 0,03 \text{ W/cm}^2$ to $q'' = 0,22 \text{ W/cm}^2$ yields a current intensity ranging from $I = 3 \text{ A}$ to $I = 9 \text{ A}$.

After analyzing the evolutions of the diameter (d), contact angle (θ), centroid height and bubble volume as a function of time, it was concluded that the variation of the imposed heat flux did not influence any of these parameters.

In order to understand the thermographic analysis performed, it is important to make the association between the parameters of the bubble dynamics and the temperature distribution through Figure 2.

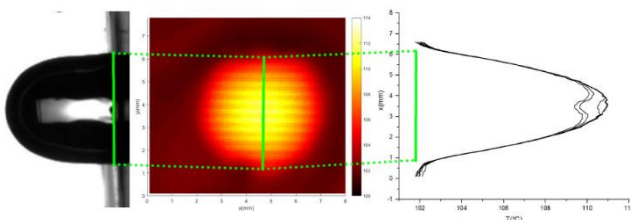


Figure 2: Example of the association between the image of a bubble enclosed in its SHF region, the corresponding temperature distribution map and the corresponding graph of the temperature evolution

This figure outlines the interconnection between the images taken from the high-speed camera, the images obtained from the IR camera and the curves corresponding to the evolution of the temperature profile. It is verified that the temperature is shown to be lower in the hydrophilic region, which is covered with liquid, and higher in the superhydrophilic region, which is covered by a thin vapor layer. However, a small temperature gradient is observed at the interface

between the superhydrophobic region and the hydrophilic region.

In order to infer about the temperature variation at the surface-liquid interface, a biphilic configuration with a superhydrophobic region with $\phi = 5,2 \text{ mm}$ was tested (Figure 3). For this larger diameter it was possible to obtain images with a greater thermal amplitude and better resolution, which in turn made possible a better thermographic analysis during the bubble formation process and for a fixed diameter.

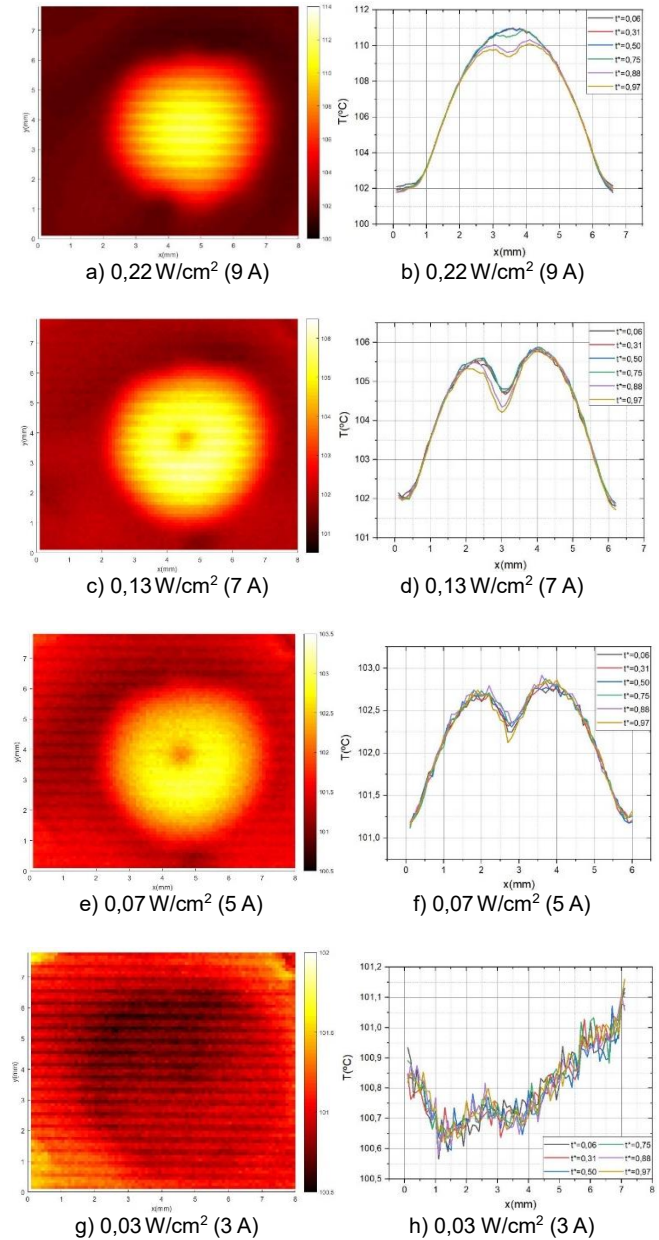


Figure 3: Comparison between thermographic images of a SHF region with $\phi = 5,2 \text{ mm}$, for $t^* = 0,5$ and for different heat fluxes, and the corresponding temperature evolution graphs, as a function of the position in the central axis of the base of a bubble (x), in which the curves correspond to several values of t^* . The temperature distribution maps of points a), c), e) and g) correspond to the graphs of the temperature evolution of points b), d), f) and h), respectively

From the initial formation phase of the bubble to its departure from the superhydrophobic region and for the currently available spatial resolution, there is no variation in the surface temperature distribution over time. As such, Figure 3 only shows thermographic images for a single stage of the bubble formation, in this case an intermediate stage ($t^* = 0,5$).

On the left of Figure 3 are presented the two-dimensional temperatures maps of the biphilic surface, obtained for four currents intensities: $I = \{3 \text{ A}; 5 \text{ A}; 7 \text{ A}; 9 \text{ A}\}$, corresponding to the heat fluxes: $q'' = \{0,03 \text{ W/cm}^2; 0,07 \text{ W/cm}^2; 0,13 \text{ W/cm}^2; 0,22 \text{ W/cm}^2\}$.

The different curves represented in the graphs to the right (b), d) and f) characterize the temperature profile along the diameter of the area of interest, for different dimensionless time instants: $t^* = \{0,06; 0,31; 0,5; 0,75; 0,88; 0,97\}$. These time values are associated to the stages of the bubble dynamics, i.e. they correspond respectively to: initial stage, hemispheric growth, vertical elongation, neck formation, necking and bubble detachment (Figure 4).

For imposed currents intensities of 5 A or higher it becomes apparent that the superhydrophobic region has a temperature higher than its surroundings during bubble formation. This is due to the lower capacity of the vapor covering this region to remove heat from the surface, compared to water in its liquid phase, i.e. the vapor has a lower heat transfer coefficient. The higher the heat flux the greater the surface superheat on the superhydrophobic area.

In the graphs of b), d) and f) there is a slight temperature inflection ($\Delta T_{max} \approx 1,5^\circ\text{C}$) in the center of the nucleation zone, which becomes proportionately less relevant as the heat flux rises. It is speculated that this decrease in temperature may be due to convection phenomena within the bubble or some instability resulting from the large diameter of the bubble.

Influence of the diameter of the superhydrophobic regions in bubble dynamics

Figure 4 shows image sequences displaying the progress in bubble formation in three superhydrophobic regions with: $\phi = \{1,5 \text{ mm}; 2,6 \text{ mm}; 5,2 \text{ mm}\}$.

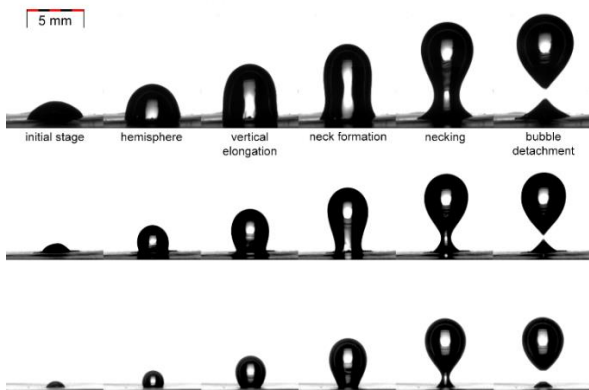


Figure 4: Sequence of bubble development images, from formation to departure, with three different diameters. From top to bottom: $\phi = 5,2 \text{ mm}$, $\phi = 2,6 \text{ mm}$ e $\phi = 1,5 \text{ mm}$

The generated bubbles follow the six phases mentioned above, regardless of the diameter of the superhydrophobic region. However, the size of the superhydrophobic region affects all these growth phases. The differences begin to be more evident on the vertical elongation phase.

The following graphs compare, in a quantitative way, the temporal evolution of the bubble diameter (Figure 5) and its contact angle (Figure 6) for superhydrophobic regions with different diameters.

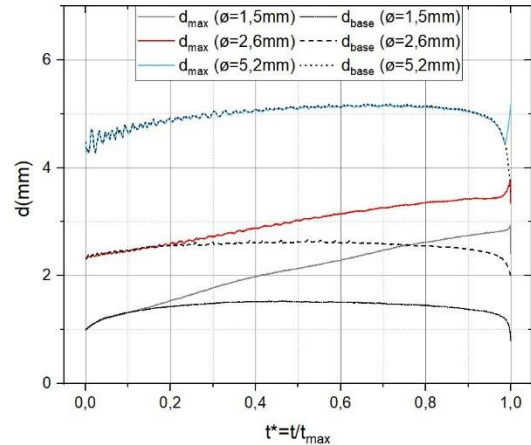


Figure 5: Evolution of the maximum bubble diameter and its base, generated in SHF regions with: $\phi = \{1,5 \text{ mm}; 2,6 \text{ mm}; 5,2 \text{ mm}\}$, for $I = 9 \text{ A}$

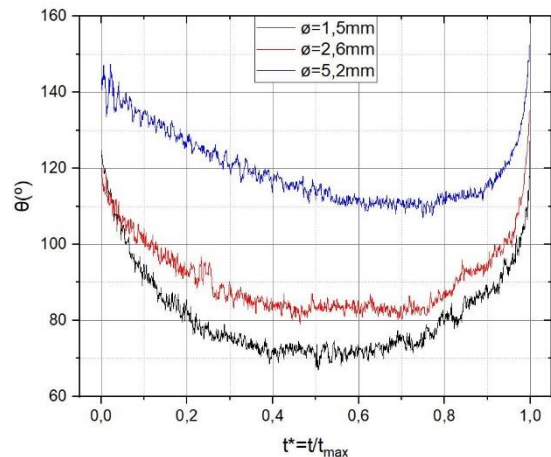


Figure 6: Evolution of the bubble dynamic contact angle, generated in SHF regions with: $\phi = \{1,5 \text{ mm}; 2,6 \text{ mm}; 5,2 \text{ mm}\}$, for $I = 9 \text{ A}$

In Figure 5, for the two smaller superhydrophobic regions, the bubble diameter exceeds its base diameter even before $t^* = 0,25$, as opposed to the bubble growing in the largest superhydrophobic region. In this last case, both the maximum temporal value of the diameter across the bubble axis and its base diameters coincide, from the initial stage to near the bubble departure, as the bubble base dictates the behavior of the dome. The diameter of the bubbles formed in the two smaller superhydrophobic regions increases linearly until the detachment. The bubble base diameter shows a similar trend regardless of the size of the superhydrophobic region. It verifies an initial increase until stabilizing momentarily, diminishing then in the

final moments of the bubble formation, until its departure.

For Figure 6, the smaller the size of the formed bubble the smaller the contact angle that it can reach throughout the development phases. The superhydrophobic region with 1,5 mm in diameter generates bubbles with angles that can reach less than 70°. In the region with 5,2 mm in diameter, the generated bubble presents angles with values always higher than 110° and in turn, the region of 2,6 mm in diameter produces bubbles with minimum angles of approximately 80°. It is also shown that, in the initial stages of bubble growth, the decrease of the bubble angle is lower for the superhydrophobic regions with higher diameters, thus complying to a slower bubble diameter growth rate. The evolution of the bubble contact angle depends on the balance between the buoyancy forces and the surface tension forces. In the absence of the surface tension component, which contributes to the necking phase, the bubbles formed in the largest superhydrophobic region tend to grow without restriction, following the diameter of the base. Consequently, these bubbles have a shape that promotes the formation of high contact angles.

From these parameters a greater focus is given to the evolution of the bubble diameter and its base diameter, particularly its relation when they reach their maximum values. Figure 7 depicts the ratio between the maximum bubble diameter (d_{max}) and its base diameter (d_{base}) as a function of the superhydrophobic regions size.

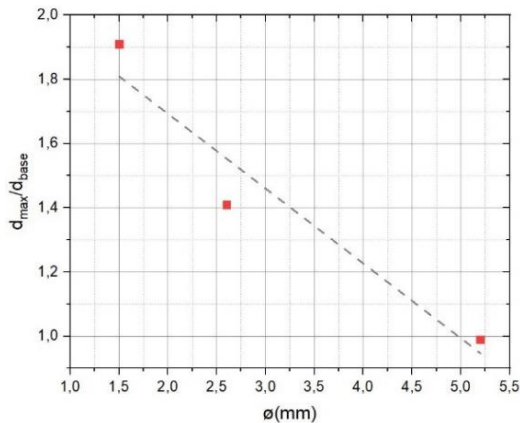


Figure 7: Ratio between the maximum bubble diameter (during detachment) and the base diameter for the three SHF regions: $\phi = \{1,5 \text{ mm}; 2,6 \text{ mm}; 5,2 \text{ mm}\}$, for $I = 9 \text{ A}$

This figure shows that although the diameter of the generated bubbles is larger for the larger superhydrophobic regions, the ratio between the maximum bubble diameter and the base diameter decreases with the increase of the size of the superhydrophobic region. This trend suggests that the larger superhydrophobic regions do not necessarily promote the formation of more evaporated mass, which in turn will condition (depending on the bubble departure frequency) the surface performance in terms of the amount of latent heat removed.

Influence of the diameter of a super-hydrophobic region in heat transmission and in the evaporated mass flux ratio

By analyzing thermographic images of the two superhydrophobic regions with the diameters $\phi = 1,5 \text{ mm}$ and $\phi = 2,6 \text{ mm}$ a reduction of the surface temperature was detected, located in the vicinity of these superhydrophobic regions with the surrounding liquid. This suggests an eventual dominance of the heat transfer mechanism in the boundary between the hydrophilic area and the superhydrophobic area, which is more noticeable in the smaller superhydrophobic regions.

The higher the superhydrophobic region, the greater the difference between the temperature in the center of this region and its boundary with the hydrophilic region, since it also increases the area covered by the vapor film. This trend is clearly visible in Figure 8, which shows a graph of the temperature profile of the three superhydrophobic regions mentioned so far, as a function of the dimensionless spatial coordinate x^* , for $t^* = 0,5$.

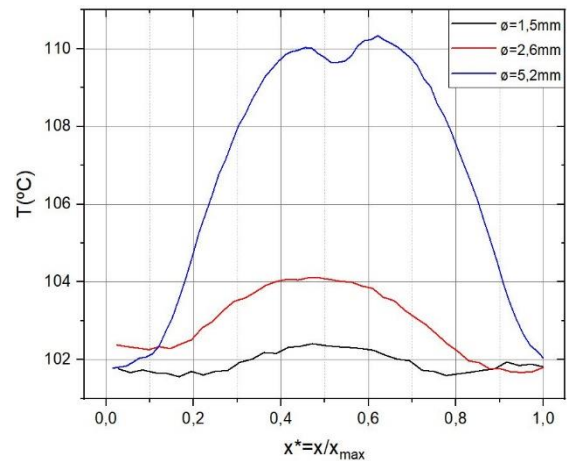


Figure 8: Temperature evolution in SHF regions with different diameters: $\phi = \{1,5 \text{ mm}; 2,6 \text{ mm}; 5,2 \text{ mm}\}$, as a function of x^* . The values were taken for $t^* = 0,5$ and for $I = 9 \text{ A}$

The general temperature gradients of the two smaller diameters are low (about 1-2°C), which together with the spatial resolution available in the thermographic images, makes it difficult to observe their occurrence along the bubble formation.

It is important to evaluate the effectiveness of each biphilic surface regarding the formation of evaporated mass, since this parameter is directly related to the latent heat removed from the surface, in pool boiling. The bubble departure frequency is also important because it allows the evaluation of evaporated flow rates.

Figure 9 shows the evaporated mass flow rate (\dot{m}) per superhydrophobic area (A_{SHF}). The graph presented in this figure clearly shows that the smaller superhydrophobic region ($\phi = 1,5 \text{ mm}$) is the one that presents a better performance, since it promotes higher evaporated mass flow rate, thus contributing positively

to the portion of latent heat that can be removed from the surface.

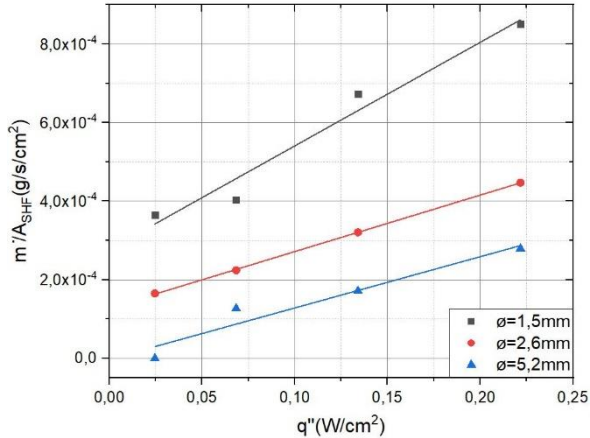


Figure 9: Comparison of evaporated mass flow rate per area in SHF regions with different diameters: $\phi = \{1,5 \text{ mm}; 2,6 \text{ mm}; 5,2 \text{ mm}\}$, as a function of the heat flux

Effect of the distance between superhydrophobic regions on bubble dynamics and temperature distribution

Three different distances (δ) were chosen among the superhydrophobic regions (Figure 10), namely: $\delta \approx \{0,5\phi, 1\phi, 2\phi\}$. The measurements used regards a distance between the periphery of each superhydrophobic region of approximately: half region diameter ($\delta = 0,5\phi$), one diameter ($\delta = 1\phi$) and two diameters ($\delta = 2\phi$). These biphilic configurations were subsequently analyzed in terms on bubble dynamics, heat transfer mechanisms and evaporated mass flux ratio. The diameter used for these superhydrophobic regions was $\phi = 1,5 \text{ mm}$.



Figure 10: Qualitative comparison between several tested distances. From left to right: $\delta = 0,5\phi$, $\delta = 1\phi$ e $\delta = 2\phi$. With $\phi = 1,5 \text{ mm}$

During the pool boiling experiments in the biphilic surfaces with $\delta = 2\phi$ there was no noticeable influence of the bubble dynamics in the thermal images. There were also no convective phenomena promoted by coalescence, in the middle of the two forming bubbles. Therefore, the synchronization does not show noteworthy results, besides the fact that the distance between regions is too large to exist interaction between the bubbles.

For the biphilic surface with $\delta = 1\phi$, the coalescence between the two bubbles is well visible when they collide in the final stages of their formation, as the diameter of both bubbles is near maximum. The influence that coalescence has on thermal imaging is also notable. The images presented in Figure 11 show the evolution of the dynamic interaction between two bubbles formed this biphilic surface and their influence

on thermographic images. The applied heat flux was $0,22 \text{ W/cm}^2$ (9 A).

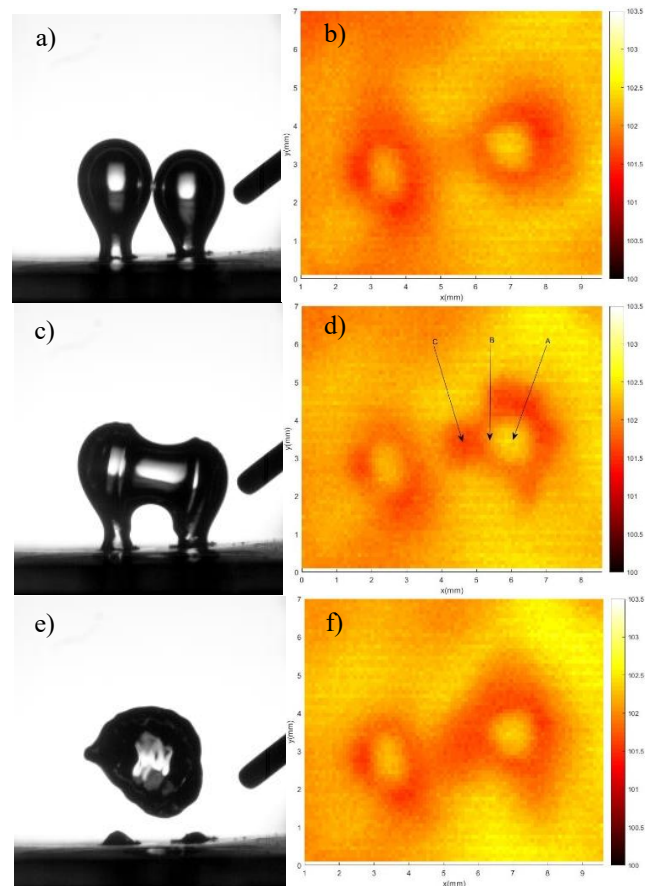


Figure 11: Synchronized images of the dynamic interaction between two bubbles in surface with $\delta = 1\phi$ and respective thermographic images. The heat flux is $0,22 \text{ W/cm}^2$. The bubble dynamics images with points a), c) and e) correspond to the temperature distribution maps of points b), d) and f), respectively. There are three interest points: center of the SHF region (A), border between hydrophilic region and SHF region (B) and hydrophilic intermediate area between the two SHF regions (C)

The showcased events occur in a time period of roughly 20 ms, which corresponds to the average transition period between the necking phase and the bubble departure, for the chosen heat flux and for the superhydrophobic region used.

In the first set of images (a) and b)), the two bubbles are presented in the necking stage. In the thermal image is possible to clearly see two hot spots surrounded by a lower temperature ring in their immediate surroundings.

In the second set of images (c) and d)), the two bubbles reach a diameter enough for both to touch and thus beginning to join. Both bubbles do not complete all their development phases, entering coalescence before their individual departure. This event leads to a sudden surface cooling due to a rapid displacement of cooler fluid, caused by the interaction between the bubbles.

In the last set of images (e) and f)) the bubbles have already taken off the surface and completed their union. In the thermal imaging the expansion of the cooling

area along the surface is mainly observed in the area between the nucleation zones. This cooling area starts to diminish during the formation of the next bubbles.

Figure 12 shows the temperature evolution at the interest points, selected in the thermographic image corresponding to the beginning of the coalescence (Figure 11 d)).

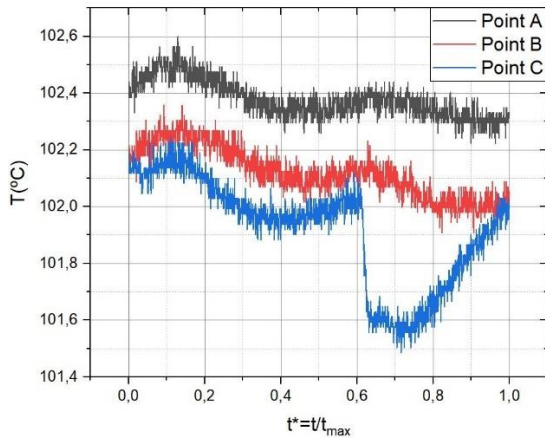


Figure 12: Variation of the temperature in interest three points for the biphilic surface with $\delta = 1\phi$

At points A and B, which correspond to the center of a nucleation zone and to its periphery respectively, there is a fairly constant temperature progression along the formation and interaction of the bubbles. Point A has a temperature of approximately 102,4°C and point B of 102,1°C.

It is at point C that significant differences in temperature are noted. There is an abrupt reduction of the temperature at $t^* \approx 0,6$, which corresponds to the moment when coalescence occurs between the two bubbles. The reduction is of approximately 0,5°C and confirms the existence of a localized surface cooling caused by the coalescing phenomena.

Concerning the biphilic configuration with $\delta = 0,5\phi$ it was noted that the distance between the two superhydrophobic regions was insufficient, since the bubbles coalesced early in the experiment and formed a larger nucleation zone. Figure 13 depicts the moment when the two bubbles get permanently attached. The coalescence between the bubbles still occurs far from the final stages of their formation since their diameter was already enough for both to collide.

This biphilic configuration is not able to be extrapolated to a multi-region pattern because it runs the risk of forming a vapor layer over the whole surface. This would cause a significant reduction in the heat transfer capacity of the surface and could even damage it due to overheating.

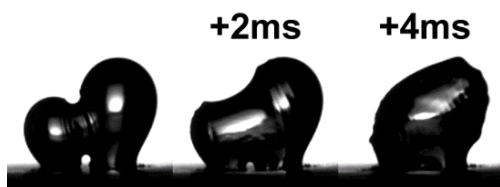


Figure 13: Coalescence phenomena for the biphilic surface with $\delta = 0,5\phi$

Effect of the distance between superhydrophobic regions on the evaporated mass flow rate

The total area used by the nucleation zones of each biphilic configuration was calculated to appraise which produces the most evaporated mass per configuration area (A_t) and per unit of time. It was estimated that this total area would be the sum of the areas of each superhydrophobic region with the hydrophilic non-coated area located between each region. The graph depicted in Figure 14 shows the evolution of the evaporated mass flux ratio as a function of the heat flux.

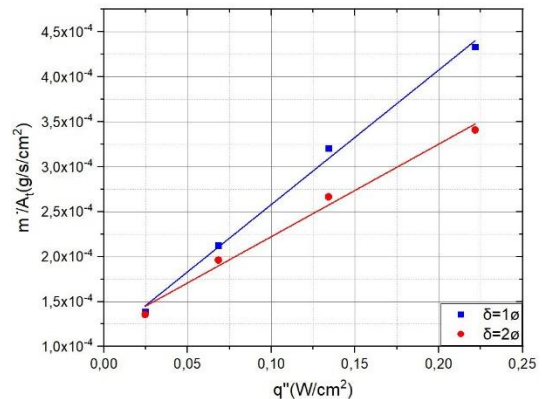


Figure 14: Comparison of the evaporated mass flux ratio of two biphilic configurations ($\delta = 2\phi$ e $\delta = 1\phi$), as a function of the heat flux

It is apparent that the biphilic configuration with $\delta = 1\phi$ presents values continuously higher than the configuration with $\delta = 2\phi$ as the imposed heat flux is increased, which can be noted by an upper. For a heat flux of $2,5 \times 10^{-2}$ W/cm² the values of \dot{m}/A_t are approximately the same but for a heat flux of 0,22 W/cm² there's already a more notable difference of around 22%. It is estimated that this difference continues to widen with the increase in the imposed heat flux.

In summary, the biphilic configuration with $\delta = 1\phi$ has a slightly lower mean bubble departure frequency, however, it has a higher evaporated mass flow rate per total area for higher imposed heat flows. The distinguishing factor is the presence of favorable coalescence in this configuration that depicts a higher periodically surface cooling.

Analysis of biphilic surfaces with three superhydrophobic regions

In order to approximate the biphilic configuration of the test surface to a complete biphilic pattern, a further superhydrophobic region was added to the two already existing ones. The distance of $\delta = 1\phi$ between the three superhydrophobic regions was used in an equilateral triangle arrangement, where each of these regions is located at one of the vertices. In this new surface the coalescence phenomenon between bubbles was again verified. The moments in which the

three bubbles begin to interfere with each other, collide and merge are explicit in Figure 15.



Figure 15: Evolution of the interaction between three bubbles with a spacing of $\delta = 1\phi$ and diameter of $\phi = 1,5$ mm

A qualitative analysis can be done via the thermographic image shown in Figure 16.

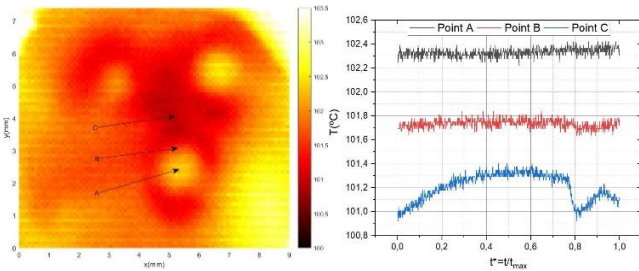


Figure 16: Thermographic image of a biphilic surface with three SHF regions (left) with $\delta = 1\phi$ and $\phi = 1,5$ mm. The heat flux is $0,22$ W/cm². Three interest points are indicated: center of the SHF region (A), border between the hydrophilic zone and the SHF zone (B) and intermediate hydrophilic zone between the three SHF regions (C). The temperature variation over time in these three points is shown on the right

The video recorded by the IR camera provides evidence to confirm the presence of a colder zone located in the central zone between the three nucleation spots. It is also apparent that this zone is impacted by the coalescence phenomena between bubbles. In this situation there's a sudden stirring in the local fluid (point C) which forces it to move between the nucleation spots and to expand the cooling area the surface momentarily. This process is verified to happen periodically as in the previous biphilic surface shown in Figure 11.

Figure 17 compares the effect of distance and number of superhydrophobic regions on the bubble departure frequency. The differences between the evolution of the frequency values of each configuration are not significant for high heat fluxes. Therefore, this last biphilic configuration also does not present a very different behavior, with a frequency only slightly higher than the other cases. It is concluded that the frequency, in this situation, is not a factor of extreme relevance in the differentiation of the biphilic surfaces, in terms of the distance between superhydrophobic regions with the same diameter or their number.

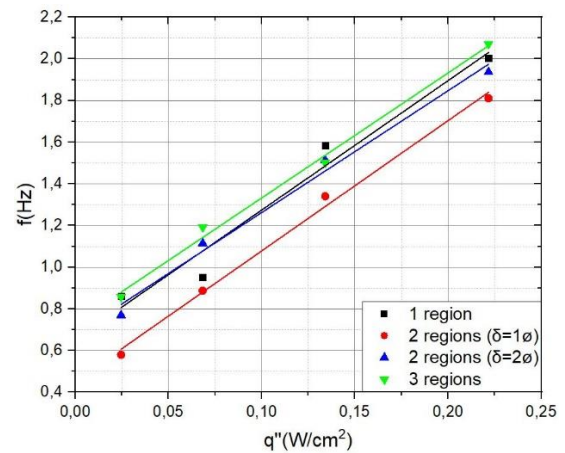


Figure 17: Comparison of the bubble departure frequency for configurations with one, two and three SHF regions and for different values of heat flux

In terms of the evaporated mass flow rate per superhydrophobic area (\dot{m}/A_{SHF}) there is a similar trend as the one depicted by the evolution of the frequency.

Conclusions

In summary, the results obtained in this work indicate that the most favorable parameters to be considered in the development of a final biphilic pattern are: a smaller diameter for the superhydrophobic region and a distance between regions approximately equal to its diameter. It was proved that a smaller diameter provides a higher bubble departure frequency and a higher evaporated mass flux ratio in terms of the total area. It was also concluded that a distance between superhydrophobic regions of approximately one region diameter allows coalescence, thus favoring convective flow and consequently cooling of the surface.

Nomenclature

A_{SHF}	Area of the SHF region (cm ²)
A_t	Total area (cm ²)
d	Bubble diameter (mm)
d_{max}	Maximum bubble diameter (mm)
d_{base}	Bubble base diameter (mm)
e	Relative error
f	Bubble departure frequency (Hz)
I	Current intensity (A)
\dot{m}	Evaporated mass flow rate (g/s)
q''	Heat flux (W/cm ²)
R_a	Surface mean roughness (μ m)
R_z	Surface peak-to-peak roughness (μ m)
t	Time (s)
t^*	Dimensionless time
T	Temperature (K)
x	Position in the SHF region axis (mm)
x^*	Dimensionless position

δ	Distance between SHF regions (mm)
ΔT_{max}	Maximum temperature gradient (K)
$\Delta\theta$	Hysteresis ($^{\circ}$)
θ	Dynamic contact angle ($^{\circ}$)
θ_a	Quasi-static advancing contact angle ($^{\circ}$)
θ_{min}	Minimum dynamic contact angle ($^{\circ}$)
θ_r	Quasi-static receding contact angle ($^{\circ}$)
θ_s	Static contact angle ($^{\circ}$)
ϕ	Diameter of the SHF regions (mm)

Acknowledgments

The author acknowledges Fundação para a Ciência e Tecnologia (FCT) for partially financing the research and supporting him with a fellowship under JICAM/0003/2017 project.

References

- [1] I. Malavasi, E. Teodori, A. S. Moita, A. L. N. Moreira, and M. Marengo, «Wettability Effect on Pool Boiling: A Review», pp. 1–61, 2018.
- [2] D. E. Kim, D. I. Yu, D. W. Jerng, M. H. Kim, and H. S. Ahn, «Review of boiling heat transfer enhancement on micro/nanostructured surfaces», *Exp. Therm. Fluid Sci.*, vol. 66, pp. 173–196, 2015.
- [3] Y. Takata, S. Hidaka, and T. Uraguchi, «Boiling feature on a super water-repellent surface», *Heat Transf. Eng.*, vol. 27, n. 8, pp. 25–30, 2006.
- [4] A. R. Betz, J. Jenkins, C. J. Kim, and D. Attinger, «Boiling heat transfer on superhydrophilic, superhydrophobic, and superbiphilic surfaces», *Int. J. Heat Mass Transf.*, vol. 57, n. 2, pp. 733–741, 2013.
- [5] H. Jo, H. Kim, H. Ahn, S. Kim, S. Kang, J. Kim and M. Kim, «The nucleate boiling heat transfer by the hydrophobic milli-dot on the silicon surface», *Trans. Korean Nucl. Soc. Spring Meet. Jeju*, pp. 567–568, 2009.
- [6] E. Teodori, T. Valente, I. Malavasi, A. S. Moita, M. Marengo, and A. L. N. Moreira, «Effect of extreme wetting scenarios on pool boiling conditions», *Appl. Therm. Eng.*, vol. 115, pp. 1424–1437, 2017.
- [7] J. Buongiorno, D. G. Cahill, C. H. Hidrovo, S. Moghaddam, A. J. Schmidt, and L. Shi, «Micro- and nanoscale measurement methods for phase change heat transfer on planar and structured surfaces», *Nanoscale Microscale Thermophys. Eng.*, vol. 18, n. 3, pp. 270–287, 2014.
- [8] T. M. Palma, «Characterization of bubble dynamics and heat transfer processes in pool boiling under extreme wetting scenarios», MSc Thesis in Mechanical Engineering, Instituto Superior Técnico, Universidade de Lisboa, 2016.
- [9] E. Teodori, «Effect of customized surface properties on pool boiling heat transfer», PhD Thesis, Instituto Superior Técnico, Universidade de Lisboa, 2017.
- [10] P. Pontes, «Thermographical analysis of interface heat transfer mechanisms , with high temporal resolution», MSc Thesis in Mechanical Engineering, Instituto Superior Técnico, Universidade de Lisboa, 2016.
- [11] A. Sielaff, «Experimental Investigation of Single Bubbles and Bubble Interactions in Nucleate Boiling.», PhD Thesis. Technische Univeristat Darmstradt, 2014.
- [12] T. Valente, «Study of the effects of wettability on pool boiling conditions in a quiescent medium», MSc Thesis in Mechanical Engineering, Instituto Superior Técnico, Universidade de Lisboa, 2015.